PrBaMn$_2$O$_{5+\delta}$ with praseodymium oxide nano-catalyst as electrode for symmetrical solid oxide fuel cells

Yiheng Gu, Yanli Zhang, Yifeng Zheng, Han Chen, Lin Ge[*], Lucun Guo[*]

College of Materials Science and Engineering, Nanjing Tech University, No. 5 Xinmofan Road, Nanjing, Jiangsu, 210009, PR China

ABSTRACT

PrBaMn$_2$O$_{5+\delta}$ (PBMO) is one of the promising electrode materials for symmetrical solid oxide fuel cells, but suffers from limited electrocatalytic activity. In this work, nanosized Pr$_6$O$_{11}$ particles were introduced into PBMO backbone on both anode and cathode as synergic catalysts and to optimize the electrode reactions. The as-prepared electrode was investigated by X-ray diffraction, H$_2$-temperature programmed reduction (H$_2$-TPR), O$_2$-temperature programmed desorption (O$_2$-TPD), X-ray photoelectron spectroscopy (XPS), field emission scanning electron microscope (FESEM) and the electrochemical measurements. After coated with Pr$_6$O$_{11}$, the cathode polarization resistance (R$_p$) of PBMO decreased from 0.25 to 0.016 Ω cm^2, the anode R$_p$ reduced from 0.46 to 0.20 Ω cm^2 and the power outputs of symmetrical cells improved by ∼75% at 800 °C. The TPR and TPD results indicate that the electrode catalytic activity was significantly promoted by Pr$_6$O$_{11}$. Furthermore, the stability tests show that PBMO with Pr$_6$O$_{11}$ is highly stable in redox conditions.

1. Introduction

Solid oxide fuel cells (SOFC) are high-efficient energy conversion devices that can directly utilize fossil fuel gas to generate electricity [1,2]. Over the past decade, a new configuration of symmetrical solid oxide fuel cells (SSOFC) with one identical material as anode and cathode was proposed [3,4]. This cell configuration provides many benefits, including simple fabrication process, good material compatibility and enhanced carbon and sulfur tolerance by reversible gas flows [5]. However, it becomes a challenge on finding proper materials to work as symmetrical electrodes, because they should be stable and simultaneously maintain sufficient activity under both oxidizing and reducing conditions [6]. Irvine and Ruiz-Morales et al. first reported the La$_{0.75}$Sr$_{0.25}$Cr$_{0.5}$Mn$_{0.5}$O$_{3-\delta}$ to be a redox-stable electrode and the symmetrical cell showed ∼500 mW cm^{-2} power outputs in pure H$_2$ at 950 °C [7,8]. Since then, many novel perovskite materials have been developed as electrode for symmetrical SOFCs which gained much attention [5,6,9,10]. For example, the Sr$_2$Fe$_{1.5}$Mo$_{0.5}$O$_{6-\delta}$ (SFM) perovskite exhibits considerably high electrical conductivity in reducing atmosphere and the σ value reaches to ∼300 S cm^{-1} at 780 °C [9]. The PrBaMn$_2$O$_{5+\delta}$ (PBMO) presents a unique layered structure with numerous oxygen vacancies and it shows high stability in sulfur-containing fuels [11]. Although these perovskites are considered as good candidates for symmetrical electrodes, cells with them are found to

operate at relatively high temperatures (> 850 °C) to achieve comparable power outputs [8,11,12].

On the other hand, a number of special approaches were applied to optimizing the electrochemical performance for symmetrical electrodes, among which included the ionic doping [13,14] and structure modification [15,16] methods. As reported by Kim et al., the electrical conductivity of PBMO can be improved by replacing partial Ba^{2+} with Ca^{2+} and the PrBa$_{0.8}$Ca$_{0.2}$Mn$_2$O$_{5+\delta}$ exhibits good durability in various hydrocarbon fuels [14]. Ding et al. fabricated a Pr$_2$NiO$_4$/Sm$_{0.2}$Ce$_{0.8}$O$_{1.9}$ composite electrode with *in-situ* exsolved nanoparticles and it showed sufficient activities for hydrogen oxidation and oxygen reduction reactions (ORR) [15]. In addition, introduction of catalysts has been reported to be another effective approach to optimizing the electrochemical performance of electrode materials, which helps to obtain additional catalytic activity toward chemical reactions [17–20]. Lee et al. prepared a non-precious Co-Ni-Mo alloy catalyst for the Sr$_2$FeMoO$_{6-\delta}$ electrode, which decreased the hydrogen binding energy and significantly influenced the hydrogen oxidation reactions (HOR) [21]. It is also reported that the praseodymium oxide is highly active to oxygen dissociation and it will result in an outstanding promotion of ORR [22,23]. But in some cases, the electrode materials could experience phase transition or structure change during these modification processes, and the symmetrical cells may not be reversible any more [3,24,25]. It is essential to optimize the electrodes and simultaneously

ensure the unique symmetry property of symmetrical SOFC.

In this work, $PrBaMn_2O_{5+\delta}$ with praseodymium oxide (Pr-PBMO) was fabricated as the electrode for intermediate-temperature symmetrical SOFCs. The Pr_6O_{11} nanoparticles were introduced into both the anode and cathode to serve as synergistic catalyst, without sacrificing the symmetry property of symmetrical cells. The morphologies, electrochemical properties, redox stability, as well as the performance mechanisms of the Pr-PBMO electrode were discussed.

2. Experimental

2.1. Powder synthesis

The $Pr_{0.5}Ba_{0.5}MnO_3$ powder was prepared by citric acid combustion method. Stoichiometric amount of $Pr(NO_3)_3\cdot6H_2O$, $Ba(NO_3)_2$ and $Mn(NO_3)_2\cdot4H_2O$ was dissolved in distilled water with citric acid and ethylene glycol added as complexing agents. The molar ratio of metal ions, citric acid and ethylene glycol was 1:3:1.5. $NH_3\cdot H_2O$ was added into the solution to adjust the pH value to ~8. After stirred for 2 h, the mixed solution was heated on a hotplate until auto-combustion occurred. The combustion products were calcined at 950 °C for 4 h to form $Pr_{0.5}Ba_{0.5}MnO_3$ perovskite.

2.2. Cell fabrication

The electrolyte substrates for half-cell tests were prepared by dry pressing method. Commercial yttria-stabilized zirconia (8-YSZ, Terio, China) powder was set in a steel mound with diameter of 20 mm and pressed at 200 Mpa to form green pullets. The electrolyte substrates for single cell tests were fabricated by tape casting technique. To prepare the slurry, YSZ powder was dispersed in ethanol-based solvent with caster oil as dispersant, dibutyl phthalate (DBP) as plasticizer, and polyvinyl butyral (PVB) as binder and the mixture was ball-milled for 24 h. The slurry was then cast on release film and dried in air at room temperature. The green tapes were cut into small pullets with diameter of 20 mm after totally dried. Both the green electrolyte pullets made by dry pressing and tape casting were sintered at 1450 °C for 2 h. Commercial $Ce_{0.9}Gd_{0.1}O_{1.95}$ (GDC_{10}, SOFCMAN, China) was screen printed on surface of the electrolyte substrates as buffer layers, followed by sintering at 1300 for 2 h. The electrode slurry was prepared by mixing PBMO powder and terpineol with weight ratio of 1:2. The slurry was then screen-printed onto both sides of the electrolyte and sintered at 1100 °C for 2 h.

For infiltrating, stoichiometric amounts of $Pr(NO_3)_3\cdot6H_2O$ nitrate was dissolved in deionized water to obtain a concentration of 1 mol L^{-1} aqueous precursor. Then the solution was dripped onto the electrode layer and infiltrated into PBMO backbone by capillary forces. The volume of solution employed in each infiltration cycle was controlled at ~10 μL by using a pipette. After infiltration, the samples were dried and calcined at 850 °C for 2 h. The samples infiltrated with 1–5 cycles were denoted as Cell #1, Cell #2,… and Cell #5, respectively. The blank sample was named as Cell #0.

2.3. Characterizations

To investigate the chemical properties of the Pr_6O_{11} infiltrated PBMO, stoichiometric amount of PBMO powder was added into the precursor solution and the mixture was calcined at 850 °C to obtain Pr_6O_{11} and PBMO compounds. One portion of the as-prepared powder was pretreated in humidified hydrogen at 800 °C and cooling down to room temperature without changing the atmosphere. Then, the reduced powder was heated again to 800 °C in air. X-ray diffraction (XRD) analysis of the pristine, annealed and re-oxidized samples were performed by an X-ray diffractometer (Rigaku, Japan). H_2-temperature programmed reduction (H_2-TPR) and O_2-temperature programmed desorption (O_2-TPD) tests were carried out by the AutoChem II 2920
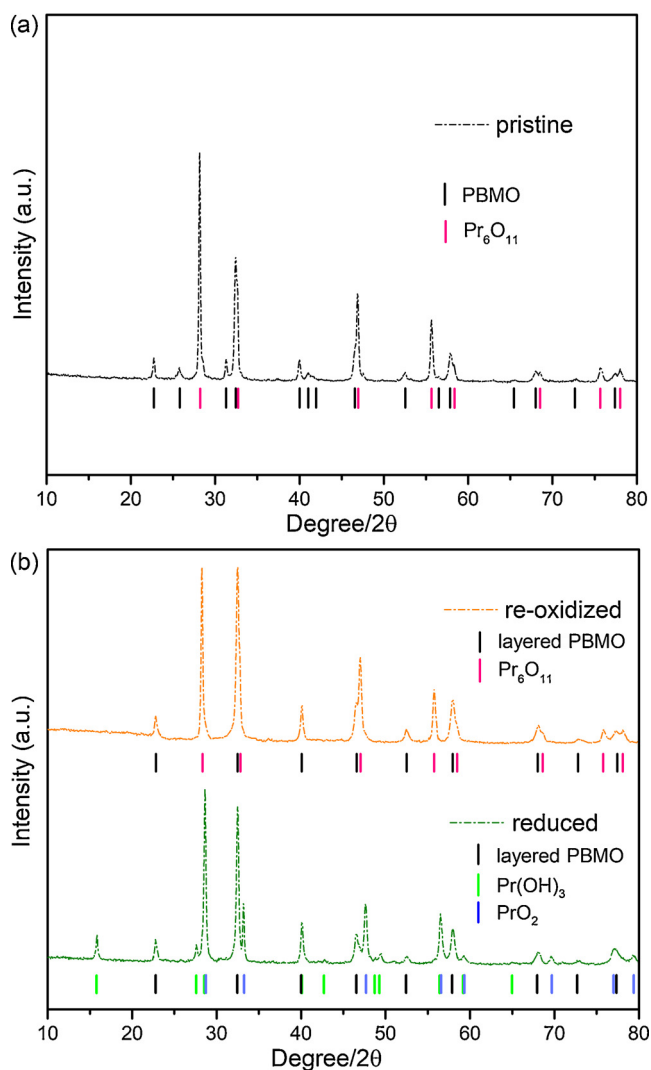
instrument (Micromeritics, the USA). X-ray photoelectron spectroscopy (XPS) analysis was conducted by an ESCALAB 250 X-ray photoelectron spectrometer (Thermo Scientific, USA) with AlKα radiation at room temperature.

The power outputs of the symmetric cells were investigated by a laboratory made testing system and the current density versus voltage (*I–V*) and current density versus power output (*I–P*) curves were obtained by a CHI660e workstation (Chenhua, Shanghai). The constant cell voltage was recorded by an IT8511 DC electronic load (ITECH, China). Hydrogen and methane were feed as fuels for single cells with gas flow rate of 100 ml/min. Meanwhile, the ambient air was used as oxidizing agent. Ag paste and Ag wires were used as current collectors and the effective electrode area is about 0.25 cm^2. The electrochemical impedance spectra (EIS) of the symmetric cells were measured with the CHI660e workstation at open circuit (OCV) condition. The frequency range for EIS measurements is from 10^5 to 0.01 Hz with an amplitude of 10 mV. The microstructure of the symmetrical cell was obtained by a field emission scanning electron microscopy (ZEISS, Germany) equipped with an energy disperse spectroscopy (EDS, Oxford Instrument).
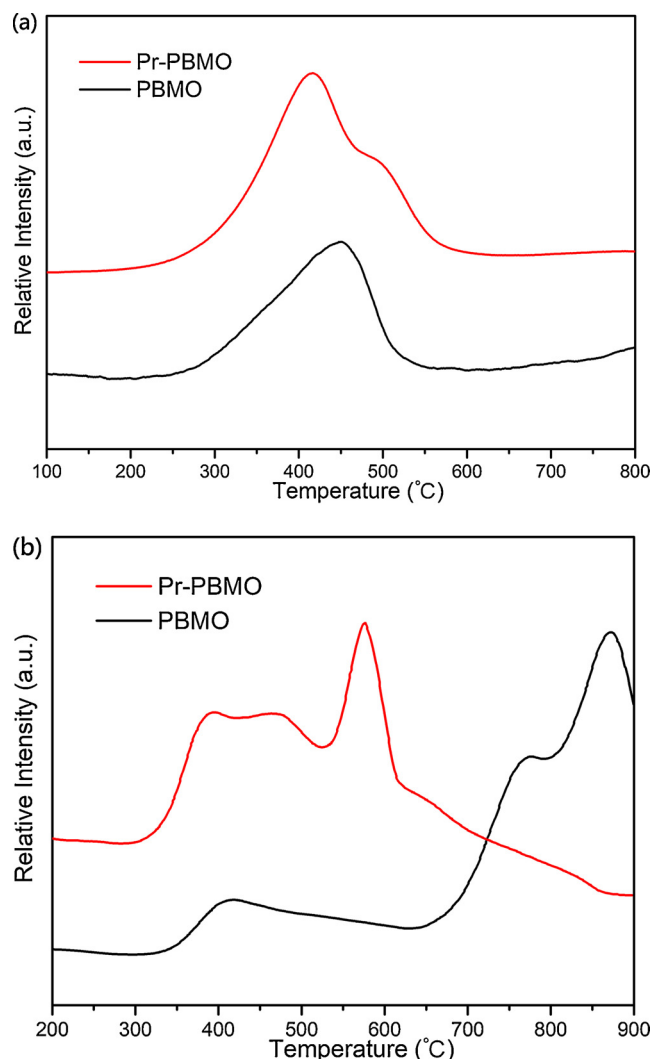

Fig. 1. (a) XRD patterns of the pristine Pr-PBMO powders; (b) XRD patterns of the reduced and re-oxidized Pr-PBMO powders.

Fig. 2. (a) H_2-TPR profiles and (b) O_2-TPD profiles of PBMO and Pr-PBMO powders.

3. Results and discussion

3.1. Powder analysis

Fig. 1a shows the XRD result of the as-synthesized Pr-PBMO mixed powder. The mixture was well indexed according to the characteristic peaks of PBMO and Pr_6O_{11}. The PBMO phase exhibits a mixed cubic and hexagonal structure after calcined in air and no interactions with Pr_6O_{11} were found. Fig. 1b presents the XRD of the samples after reduced in hydrogen and re-oxidized in air at 800 °C. In comparison, the PBMO in reduced sample presents a tetragonal structure, implying that phase change between disordered $Pr_{0.5}Ba_{0.5}MnO_{3-\delta}$ and layered $PrBaMn_2O_{5+\delta}$ occurred during reduction process. When the sample was re-oxidized in air at 800 °C, the PBMO still remained the layered structure ($PrBaMn_2O_{6-\delta}$). Similar results were also reported in previous studies [11,27]. In addition, PrO_2 and $Pr(OH)_3$ are observed from the reduced sample. It is probably because that the overall annealing process was set in humidified hydrogen atmosphere and the Pr_6O_{11} reacted with H_2O when it was cooling down to room temperature. It is reported that the Pr_6O_{11} can be denoted as a mixture of 4 mol of PrO_2 and 1 mol of Pr_2O_3 and the P_2O_3 will react with H_2O to form $Pr(OH)_3$ even when exposed in ambient air [27]. And the $Pr(OH)_3$ will decomposition and turn back to oxides when it is heated to high temperatures [28]. As shown, when the sample was re-oxidized in air at 800 °C, only the
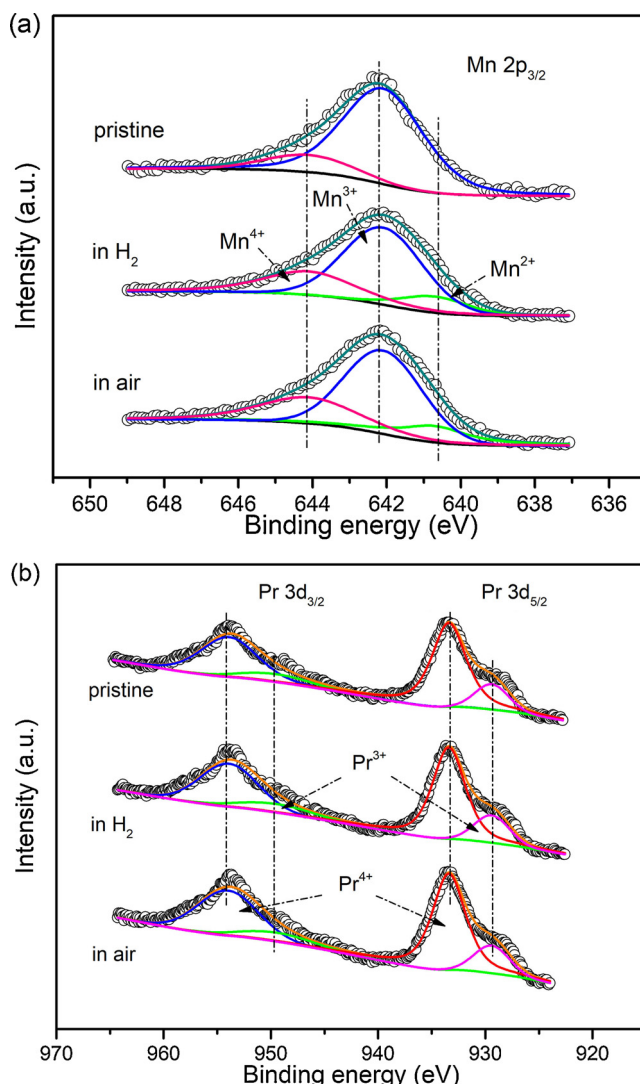

Fig. 3. (a) XPS spectra of Mn 2p in Pr-PBMO before and after ageing tests; (b) XPS spectra of Pr 3d in Pr-PBMO before and after ageing tests.

Pr_6O_{11} and layered PBMO are observed. To conclude, the Pr-PBMO electrode material presents a stable mixture of Pr_6O_{11} and layered PBMO in reducing and oxidizing atmospheres.

Fig. 2a shows the H_2-TPR profile of the PBMO and Pr-PBMO samples. The hydrogen consumption peak of PBMO is observed at ~470 °C while the peak for Pr-PBMO shifts to a lower temperature range (~410 °C), and the consumption peak area also rises. This result probably suggest that the Pr-PBMO solids contains more labile oxygen than the PBMO on surface, which is expected to accelerate the hydrogen reduction reactions on electrode [12,13]. The related O_2-TPD patterns of PBMO and Pr-PBMO are illustrated in Fig. 2b. The broad peaks observed at temperatures above 750 °C for PBMO represent the desorption of bulk oxygen, which reflects the bulk oxygen mobility inside material [29,30]. By comparison, the Pr-PBMO not only possess the bulk oxygen peaks at ~580 °C but also shows obvious off peaks within the lower temperature range of 370–480 °C. This result can be attributed to the liberation of the chemisorbed oxygens on particle surface, which suggests that the Pr-PBMO contains larger concentration of oxygen vacancies on surface and higher exchange capacity between surface oxygens and bulk oxygens [29,31].

In particular, the Pr-PBMO powder was successively treated in H_2 and in air at 800 °C for 10 h to examine the chemical stability in redox conditions. The XRD patterns (Fig. S1) after the ageing tests can be
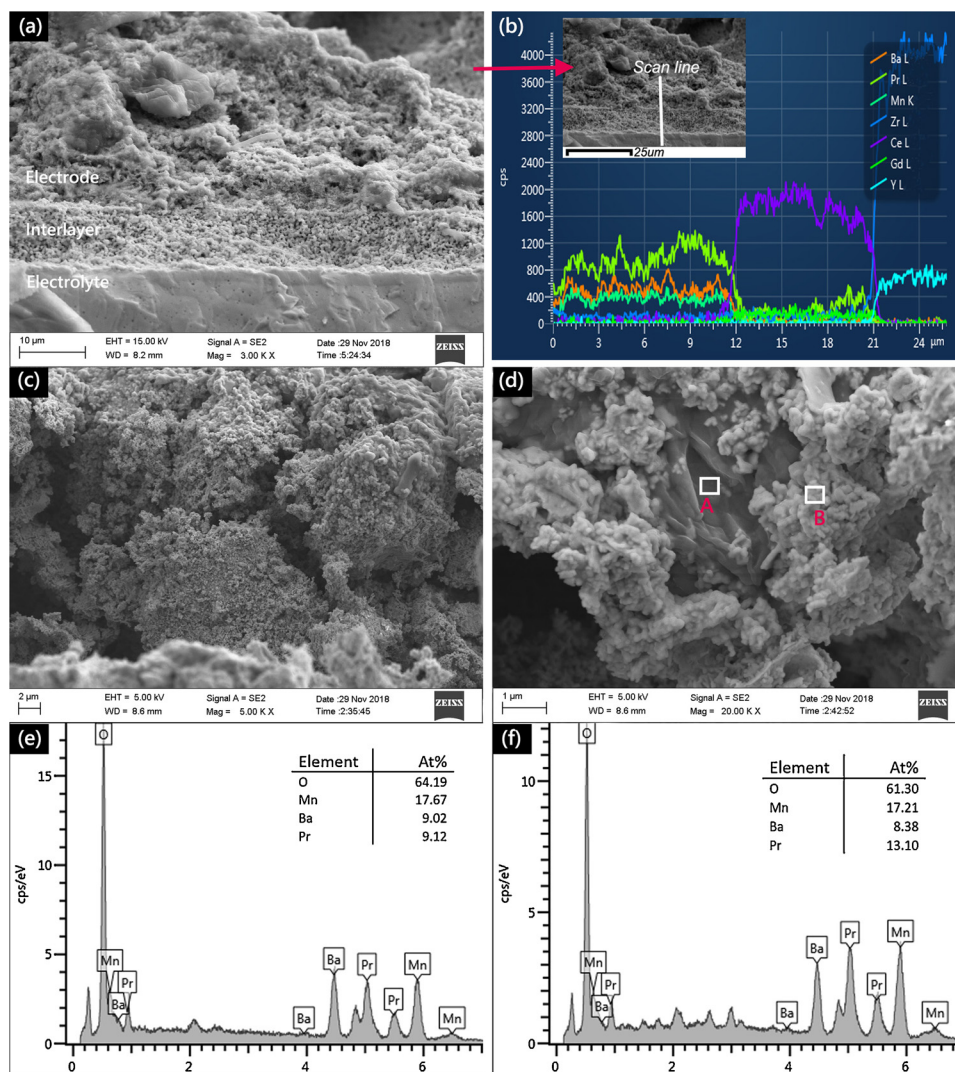
Fig. 4. (a) Cross-sectional SEM images of the Pr-PBMO electrode; (b) the EDS line scan profile near the interface; (c–d) the magnified detail of electrode surface; EDS spectrum of the selected (e) area A and (f) area B in Fig. 4d.

clearly indexed as a mixture of layered PBMO and Pr_6O_{11}, indicating the phase stability of this material. XPS was carried out to investigate the possible valence state changes in Pr-PBMO before and after the tests. The XPS spectrum of Mn 2p is shown in Fig. 3a. The deconvoluted peaks at binding energy of 640.7, 642.3 and 644.1 eV belong to Mn $2p_{3/2}$ at 2^+, 3^+ and 4^+ valences, respectively [29,32]. The specific ratio of Mn in different valences are listed in Table S1. It is found that the ratio of Mn^{2+} increases and the amount of Mn^{3+} and Mn^{4+} decrease after tested in H_2. The reduction of Mn^{4+} to Mn^{3+} and Mn^{3+} to Mn^{2+} in PBMO suggest the formation of oxygen vacancies in order to maintain electroneutrality [11,32]. After re-oxidization, the amount of Mn^{2+} decrease slightly, which probably means that a number of Mn^{2+} ions turn back into higher valence states due to the higher oxygen concentration of air [26]. Fig. 3b shows the XPS spectrum of Pr 3d in Pr-PBMO. Two sets of spin-orbit multiples at 954 and 934 eV are observed, which represent the $3d_{3/2}$ and $3d_{5/2}$ ionization of Pr, respectively. The signals at 929.4 and 949.5 eV are assigned to Pr^{3+}, and the signals at 933.4 and 953.9 eV are attributed to Pr^{4+} [33,34]. The valence state distribution of Pr among different samples are almost unchanged (Table S2), indicating the redox stability of the Pr_6O_{11} synergistic catalyst. Besides, the XPS results of PBMO without Pr_6O_{11} are provided in Fig. S2, Table S3 and S4.

3.2. Half-cell measurements

The morphology of the freshly reduced Pr-PBMO electrode is presented in Fig. 4. As shown in Fig. 4a, the porous electrode layer is well attached to the GDC interlayer based on a dense YSZ support. The EDS line scan profile in Fig. 4b shows that the element Pr mainly distributes at the range of 0–12 μm, indicating that the Pr_6O_{11} catalyst are limited in the PBMO backbone during infiltration. No obvious element diffusion is found at the interlayers either. The magnified views in Fig. 4c and d suggest that the Pr_6O_{11} particles are uniformly coated on PBMO surface and the average particle size is at ∼ 300 nm. The microstructure of the blank cell is also provided as a contrast (Fig. S3). Fig. 4e and f show the EDS spectrum of the two selected regions in Fig. 4d, respectively. The elementary composition in region A is consistent with the stoichiometric ratio of $PrBaMn_2O_{5+\delta}$ while higher content of Pr element is observed in region B, implying the presence of Pr_6O_{11} on the PBMO surface.

To evaluate the effect of catalyst contents on electrode performance, EIS of cells with different infiltration cycles were measured in hydrogen and air at 800 °C. The fitted results and the corresponding equivalent circuit are provided in Fig. S4. In the equivalent model, L represents the inductance and R_{ohm} equals to the total ohmic resistance. Meanwhile, $(R_H Q_H)$ and $(R_L Q_L)$ represent the constant phase elements and polarization resistances (R_p) at high and low frequency, respectively [35].
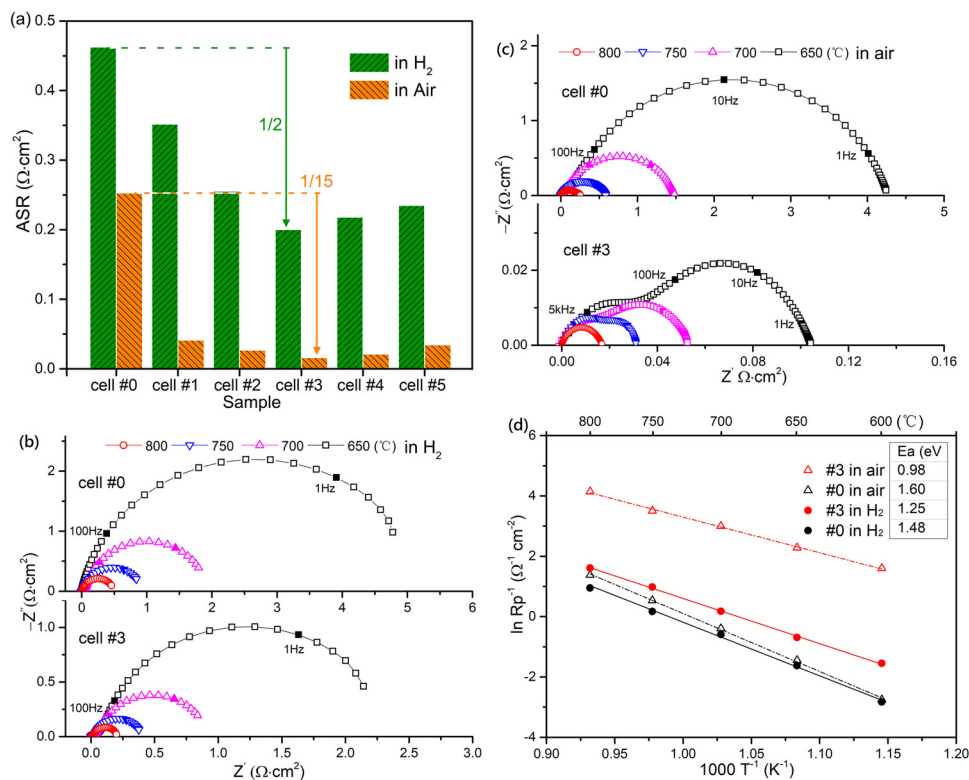
Fig. 5. (a) ASR values for the cells with different infiltration cycles; (b) EIS of Cell#0 and Cell#3 measured at 650–800 °C in H_2; (c) EIS of Cell#0 and Cell#3 measured at 650–800 °C in Air; (d) the corresponding Arrhenius plots of Cell#0 and Cell#3.

Table 1
Polarization resistances of the symmetrical electrodes in literatures.

Electrode	Temperature (°C)	Electrolyte	Interfacial polarization resistance ($\Omega\ cm^2$)		Ref.
			in air	in H_2	
LSCM/YSZ	850	YSZ	0.27	0.34	[8]
SFM	800	LSGM[a]	0.24	0.27	[9]
$PrBaMn_{1.5}Fe_{0.5}O_{5+\delta}$	800	LSGM	0.22	0.68	[13]
PBMO/YSZ	800	YSZ	0.12	0.26	[16]
$SmBaMn_2O_{5+\delta}$	850	LSGM	0.13	0.57	[37]
Pr-PBMO	800	YSZ	0.016	0.20	this work

[a] $La_{0.9}Sr_{0.1}Ga_{0.8}Mg_{0.2}O_{3-\delta}$.

The R_{ohm} of the Nyquist plots are normalized to zero to highlight the size differences between polarization resistance arcs. Fig. 5a shows the area specific resistance (ASR) values calculated from the EIS of different cells. As shown, the ASR values are dramatically reduced for all the infiltrated samples. The ASR for cell#3 is 0.20 $\Omega\ cm^2$ in H_2 and 0.016 $\Omega\ cm^2$ in air at 800 °C, which is only 1/2 and 1/15 to those of cell#0, indicating that three cycles may be optimal. The increased ASRs for cell#4 and 5 may be due to the overloading of catalyst in electrode backbone.

Fig. 5b shows the EIS measured from 650 to 800 °C in hydrogen for cell#0 and cell#3. The anode R_p for cell#0 are 0.46, 0.88, 1.92 and 4.98 $\Omega\ cm^2$ at 800, 750, 700 and 650 °C, respectively. By comparison, the values for cell#3 are 0.20, 0.38, 0.85 and 2.2 $\Omega\ cm^2$, which shows decreases of 54%, 62%, 55% and 56%, respectively. Fig. 5c shows the EIS of the cells that measured in air. The cathode R_p for cell#0 are 0.25, 0.60, 1.49 and 4.25 $\Omega\ cm^2$ at 800, 750, 700 and 650 °C, respectively. While the values for cell#3 at corresponding temperatures are only 0.016, 0.031, 0.052 and 0.104 $\Omega\ cm^2$, which are 1/15, 20/1, 1/30 and 1/40 to those of cell#0. The above results demonstrate that both the anode and cathode performances of PBMO were dramatically improved after infiltration. Pr_6O_{11} can boost the hydrogen oxidation and oxygen

reduction activities on Pr-PBMO electrode. In addition, the anode performance for Pr-PBMO is better than that of some prevailing perovskite electrodes, such as $Sr_2Fe_{1.5}Mo_{0.5}O_{6-\delta}$ (0.27 $\Omega\ cm^2$ at 800 °C in wet H_2) [9] and $PrBaMn_{1.5}Fe_{0.5}O_{5+\delta}$ (0.68 $\Omega\ cm^2$ at 800 °C in 5% H_2) [13], and the cathode performance is even superior to the conventional $La_{0.6}Sr_{0.4}Co_{0.8}Fe_{0.2}O_{3-\delta}$ cathode (0.064 $\Omega\ cm^2$ at 800 °C in air) [36]. The R_p results for several symmetrical electrodes in literatures are listed in Table 1. Fig. 5d presents the Arrhenius plots of the PBMO and Pr-PBMO in H_2 and air. The activation energy (Ea) for Pr-PBMO cathode is about 0.98 eV, which is much lower than that of PBMO (1.6 eV). It means that the Pr-PBMO electrode has low potential barriers of reaction and it may achieve higher performance at reduced temperatures.

To get more insight into the ORR process on electrode, cell#0 and cell#3 were further tested under different oxygen pressures at 750 °C and the corresponding EIS were recorded on Fig. 6a and b. The data were fitted by the same equivalent circuit as above (Fig. S4). The nonlinear dependence of polarization resistance (R_p) with the oxygen partial pressure ($p(O_2)$) can be represented by the expression below:

$$R_P \propto p(O_2)^{-n} \tag{1}$$

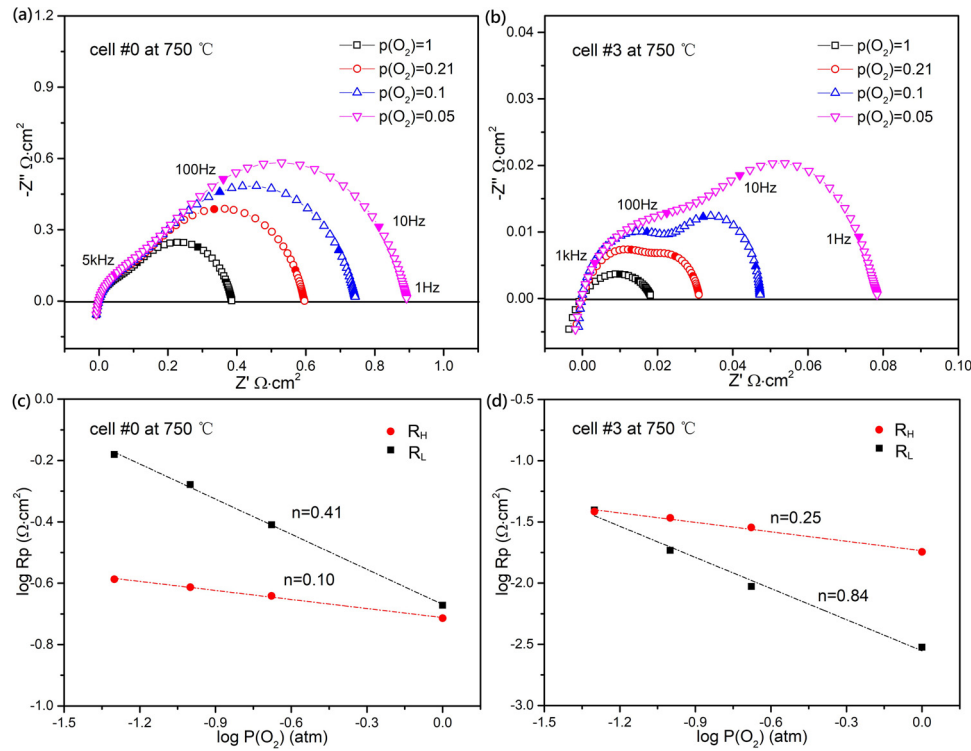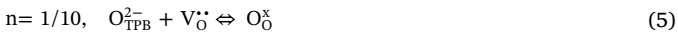According to the literatures, reaction steps involved in the ORR at

Fig. 6. (a,b) EIS of Cell#0 and Cell#3 at 750 °C under various oxygen partial pressures; (c–d) p(O₂) dependence of the polarization resistance (R_P) for Cell#0 and Cell#3.

Table 2
Fitting polarization resistance results of cell#0 and cell#3 at 750 °C under different oxygen partial pressure.

Oxygen partial pressure (atm)	Cell#0		Cell#3	
	R_H (Ω cm²)	R_L (Ω cm²)	R_H (Ω cm²)	R_L (Ω cm²)
1	0.193	0.213	1.78E-02	2.99E-03
0.21	0.228	0.389	2.85E-02	9.40E-03
0.1	0.244	0.527	3.41E-02	1.85E-02
0.05	0.259	0.661	3.84E-02	3.95E-02

electrode can be drawn from the variation of n-values [38,39].

$$n = 1, \quad O_2(g) \Leftrightarrow O_{2,ads} \tag{2}$$

$$n = 1/2, \quad O_{2,ads} \Leftrightarrow 2O_{ads} \tag{3}$$

$$n = 1/4, \quad O_{ads} + 2e' + V_O^{\bullet\bullet} \Leftrightarrow O_O^x \tag{4}$$

$$n = 1/10, \quad O_{TPB}^{2-} + V_O^{\bullet\bullet} \Leftrightarrow O_O^x \tag{5}$$

The p(O₂) dependence of R_p for cell#0 and cell#3 are presented in Fig. 6c and d. In high-frequency region (R_H), the slopes of cell#0 and cell#3 are 0.1 and 0.25. It suggests that the R_H of cell#0 is related to the oxygen ion transfer process from triple phase boundary (TPB) to the electrolyte (Eq. (5)) and the R_H of cell#3 is connected with the charge transfer process of oxygen ions (Eq. (4)) [38]. In case of the low-frequency arcs (R_L), n-values of 0.41 and 0.84 are observed. It means that the surface diffusion of adsorbed oxygen (Eq. (3)) and the oxygen adsorption-desorption process (Eq. (1)) become the rate limiting steps for cell#0 and cell#3, respectively [39]. In summary, the higher frequency arcs can be attributed to the charge transfer process, whereas the lower frequency arcs are ascribed to the non-charge transfer process. In addition, the specific fitted EIS data are listed in Table 2. It can be found that the variation of R_L between these two cells is more pronounced than that of R_H. This result indicates that the Pr₆O₁₁ mainly affects the oxygen diffusion and surface exchange processes, which is consistent with the O₂-TPD result.

3.3. Single cell performances

Single cell tests with hydrogen and methane fuels were performed to evaluate the power generating performances of PBMO and Pr-PBMO cells. The I–V and I–P curves obtained at 800 °C are shown in Fig. 7a and c. The OCV of the cells measured with hydrogen are approximately 1.1 V, close to the value calculated from the Nernst equation. The peak power density of cell with Pr-PBMO electrode reaches to 423 mWcm⁻², which is 1.7 times of that achieved by PBMO (245 mWcm⁻²). In case of the cells with CH₄ fuel, the peak power density is about 134 mWcm⁻² for PBMO and 227 mWcm⁻² for Pr-PBMO, demonstrating an improvement of ~70%. The Nyquist plots obtained at OCV condition are recorded on Fig. 7b and d. It is found that the R_p reduces significantly while the R_ohm remains almost unchanged. Therefore, the improved power outputs of the symmetrical cells are mainly due to the decrease of R_p, which is strongly related to the electrode kinetics. Furthermore, the power density could be improved if the cells employ thinner electrolytes with reduced ohmic resistance.

The cell voltage versus time in a constant current density mode (0.42 A cm⁻², 750 °C) was recorded to evaluate the durability for Pr-PBMO (Fig. 8). The cell voltage stabilized at ~0.56 V for over 80 h when the cell was feed with hydrogen. Subsequently, the fuel gas was switched to methane and the cell kept running for another 50 h. No obvious degradation of cell voltage was found during the operations in methane, indicating the carbon tolerance of Pr-PBMO. The microstructure of the electrode after the short-tern running was also examined (Fig. S4). The morphology and elementary composition at anode and cathode show no significant changes compared to those for the fresh sample (Fig. 4), which means that the Pr-PBMO is stable in the real working condition of SOFC.
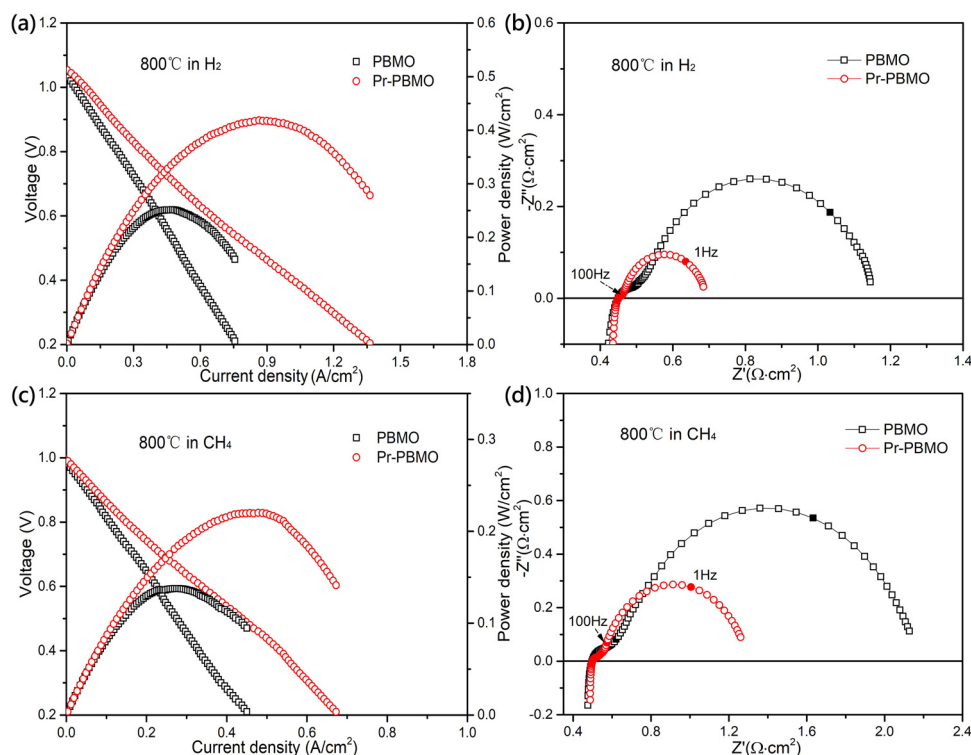
Fig. 7. (a) *I–V* and *I–P* curves and (b) the Nyquist plots of the symmetrical cells with PBMO and Pr-PBMO electrode tested in humidified H_2; (c) *I–V* and *I–P* curves and (d) the Nyquist plots of the symmetrical cells tested in humidified CH_4.
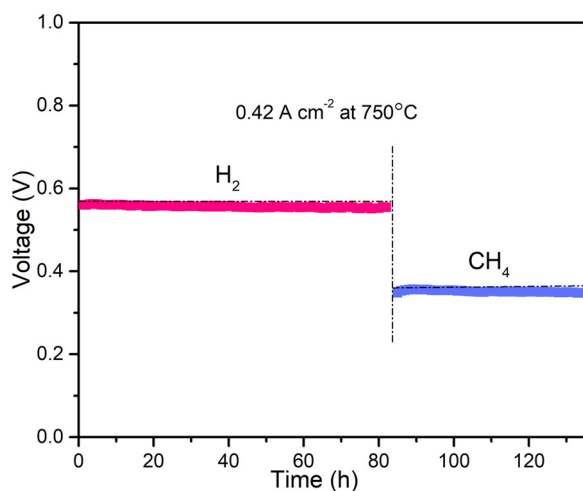
Fig. 8. Durability test in constant current density mode with hydrogen and methane as fuel.

3.4. Performance mechanisms

The performance mechanism of SOFC is well known as follows: the oxygen molecule adsorbed on the cathode and decomposed to O^{2-} (Eq. (2–5)); the oxygen ions transport through the electrolyte and reach to the anode; the fuel gas molecules, H_2 or CH_4 for example, decompose on the anode and react with O^{2-} to form H_2O (Eq. (6,7)) [40,41].

$$H_2 + O^{2-} \rightarrow H_2O + 2e^- \tag{6}$$

$$CH_4 + 4O^{2-} \rightarrow CO_2 + 2H_2O + 8e^- \tag{7}$$
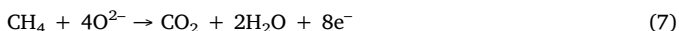
The kinetics of electrode are dependent not only on materials but also on the microstructures. As schematically illustrated in Fig. 9, the nanosized Pr_6O_{11} particles are coated on surface of PBMO, providing the electrode with extra reaction active sites. The BET results demonstrate the improved specific surface area of Pr-PBMO (Table S5). At anode side (Fig. 9b), the labile oxygens on Pr_6O_{11} are trend to react with the hydrogen. The bulk oxygen in PBMO will immigrate to the surface through oxygen vacancies and supply for the HOR process (Eq. (6)), which is verified by the results in Fig. 2a. Similar synergetic effect of praseodymium oxide on hydrogen absorption and methane reforming was also reported in some previous studies [18,42]. In case of the cathode (Fig. 9c), the oxygen molecules are more likely to absorbed on the electrode surface due to the presence of Pr_6O_{11} (Eq. (2, 3)), which is supported by the O_2-TPD and EIS results. It is also reported that the oxygen vacancy formation energy of PrO_2 is much lower than the perovskite cathodes [23]. The Pr_6O_{11} catalyst strongly facilitates the incorporation and dissociation of oxygen molecule, leading to the enhancement of ORR on Pr-PBMO. The cooperative mechanism between these two sides probably explains the significant improvements of cell performance.

4. Conclusion

In this paper, a novel Pr-PBMO electrode with Pr_6O_{11} nano-catalyst was investigated for symmetrical SOFC. This electrode not only shows superior activity toward HOR and ORR but also is highly stable in the reducing and oxidizing atmospheres. The power outputs of Pr-PBMO cell are significantly improved compared to those of the PBMO cell, which is mainly attributed to the synergic catalytic effect of the Pr_6O_{11} on fuel oxidation and oxygen reduction. Besides, no obvious degradation was observed after the cell underwent a short-term durability test in the hydrogen and methane. These results demonstrate the vital role of high-efficient catalysts on the performance of symmetrical SOFCs.
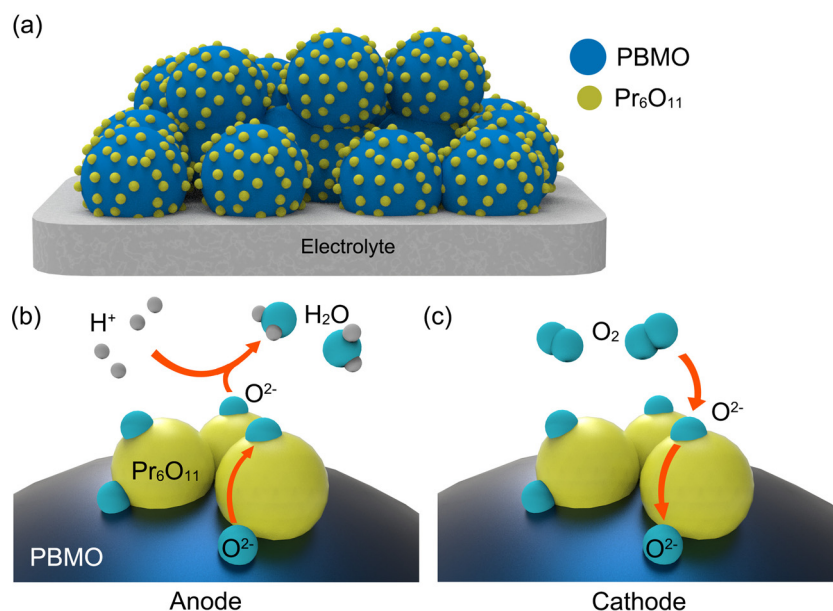
Fig. 9. (a) Schematic for the microstructure of the Pr-PBMO electrode; (b,c) Schematic illustrations of the performance mechanism on anode and cathode.

Appendix A. Supplementary data

Supplementary material related to this article can be found, in the online version, at doi:https://doi.org/10.1016/j.apcatb.2019.117868.

References

[1] S.C. Singhal, Solid oxide fuel cells for power generation. Wiley Interdisciplinary Reviews, Energy Environ. 3 (2014) 179–194.
[2] H. Dai, H. Kou, H. Wang, L. Bi, Electrochemical performance of protonic ceramic fuel cells with stable BaZrO$_3$-based electrolyte: a mini-review, Electrochem. commun. 96 (2018) 11–15.
[3] C. Su, W. Wang, M. Liu, M.O. Tadé, Z. Shao, Progress and prospects in symmetrical solid oxide fuel cells with two identical electrodes, Laser Phys. Rev. 5 (2015).
[4] J.C. Ruiz-Morales, D. Marrero-López, J. Canales-Vázquez, J.T.S. Irvine, Symmetric and reversible solid oxide fuel cells, RSC Adv. 1 (2011).
[5] J. Zhou, T.-H. Shin, C. Ni, G. Chen, K. Wu, Y. Cheng, et al., In situ growth of nanoparticles in layered perovskite La$_{0.8}$Sr$_{1.2}$Fe$_{0.9}$Co$_{0.1}$O$_{4-\delta}$ as an active and stable electrode for symmetrical solid oxide fuel cells, Chem. Mater. 28 (2016) 2981–2993.
[6] W. He, X. Wu, F. Dong, M. Ni, A novel layered perovskite electrode for symmetrical solid oxide fuel cells: PrBa(Fe$_{0.8}$Sc$_{0.2}$)$_2$O$_{5+\delta}$, J. Power Sources 363 (2017) 16–19.
[7] J.C. Ruiz-Morales, J. Canales-Vázquez, J. Peña-Martínez, D.M. López, P. Núñez, On the simultaneous use of La$_{0.75}$Sr$_{0.25}$Cr$_{0.5}$Mn$_{0.5}$O$_{3-\delta}$ as both anode and cathode material with improved microstructure in solid oxide fuel cells, Electrochim. Acta 52 (2006) 278–284.
[8] D.M. Bastidas, S. Tao, J.T. Irvine, A symmetrical solid oxide fuel cell demonstrating redox stable perovskite electrodes, J. Mater. Chem. 16 (2006) 1603–1605.
[9] Q. Liu, X. Dong, G. Xiao, F. Zhao, F. Chen, A novel electrode material for symmetrical SOFCs, Adv Mater. 22 (2010) 5478–5482.
[10] C. Li, W. Wang, N. Zhao, Y. Liu, B. He, F. Hu, et al., Structure properties and catalytic performance in methane combustion of double perovskites Sr$_2$Mg$_{1-x}$Mn$_x$MoO$_{6-\delta}$, Appl. Catal. B 102 (2011) 78–84.
[11] S. Sengodan, S. Choi, A. Jun, T.H. Shin, Y.W. Ju, H.Y. Jeong, et al., Layered oxygen-deficient double perovskite as an efficient and stable anode for direct hydrocarbon solid oxide fuel cells, Nat. Mater. 14 (2015) 205–209.
[12] Y.-F. Sun, Y.-Q. Zhang, B. Hua, Y. Behnamian, J. Li, S.-H. Cui, et al., Molybdenum doped Pr$_{0.5}$Ba$_{0.5}$MnO$_{3-\delta}$ (Mo-PBMO) double perovskite as a potential solid oxide fuel cell anode material, J. Power Sources 301 (2016) 237–241.
[13] L. Zhao, K. Chen, Y. Liu, B. He, A novel layered perovskite as symmetric electrode for direct hydrocarbon solid oxide fuel cells, J. Power Sources 342 (2017) 313–319.
[14] S. Choi, S. Sengodan, S. Park, Y.W. Ju, J. Kim, J. Hyodo, et al., A robust symmetrical electrode with layered perovskite structure for direct hydrocarbon solid oxide fuel cells: PrBa$_{0.8}$Ca$_{0.2}$Mn$_2$O$_{5+\delta}$, J. Mater. Chem. A Mater. Energy Sustain. 4 (2016) 1747–1753.
[15] Z. Gao, X. Ding, D. Ding, L. Ding, S. Zhang, G. Yuan, Infiltrated Pr$_2$NiO$_4$ as promising bi-electrode for symmetrical solid oxide fuel cells, Int. J. Hydrogen Energy 43 (2018) 8953–8961.

[16] Y. Gu, Y. Zhang, L. Ge, Y. Zheng, H. Chen, L. Guo, YSZ electrolyte support with novel symmetric structure by phase inversion process for solid oxide fuel cells, Energy Convers. Manage. 177 (2018) 11–18.
[17] C. Solís, M. Balaguer, F. Bozza, N. Bonanos, J.M. Serra, Catalytic surface promotion of highly active La$_{0.85}$Sr$_{0.15}$Cr$_{0.8}$Ni$_{0.2}$O$_{3-\delta}$ anodes for La$_{5.6}$WO$_{11.4-\delta}$ based proton conducting fuel cells, Appl. Catal. B 147 (2014) 203–207.
[18] S. Zinatloo-Ajabshir, Z. Salehi, O. Amiri, M. Salavati-Niasari, Simple fabrication of Pr$_2$Ce$_2$O$_7$ nanostructures via a new and eco-friendly route; a potential electrochemical hydrogen storage material, J. Alloys. Compd. 791 (2019) 792–799.
[19] F.S. Razavi, M.S. Morassaei, A. Salehabadi, M. Ghiyasiyan-Arani, M. Salavati-Niasari, Structural characterization and electrochemical hydrogen sorption performances of the polycrystalline Ba$_2$Co$_9$O$_{14}$ nanostructures, J. Alloys. Compd. 777 (2019) 252–258.
[20] M. Ghiyasiyan-Arani, M. Salavati-Niasari, Effect of Li$_2$CoMn$_3$O$_8$ nanostructures synthesized by a combustion method on montmorillonite K10 as a potential hydrogen storage material, J. Phys. Chem. C 122 (2018) 16498–16509.
[21] M.K. Rath, K.-T. Lee, Superior electrochemical performance of non-precious Co-Ni-Mo alloy catalyst-impregnated Sr$_2$FeMoO$_{6-\delta}$ as an electrode material for symmetric solid oxide fuel cells, Electrochim. Acta 212 (2016) 678–685.
[22] D.A. Osinkin, S.M. Beresnev, N.M. Bogdanovich, Influence of Pr$_6$O$_{11}$ on oxygen electroreduction kinetics and electrochemical performance of Sr$_2$Fe$_{1.5}$Mo$_{0.5}$O$_{6-\delta}$ based cathode, J. Power Sources 392 (2018) 41–47.
[23] H. Chen, Z. Guo, L.A. Zhang, Y. Li, F. Li, Y. Zhang, et al., Improving the Electrocatalytic Activity and Durability of the La$_{0.6}$Sr$_{0.4}$Co$_{0.2}$Fe$_{0.8}$O$_{3-\delta}$ Cathode by Surface Modification, ACS Appl. Mater. Interfaces 10 (2018) 39785–39793.
[24] G. Yang, W. Zhou, M. Liu, Z. Shao, Enhancing electrode performance by exsolved nanoparticles: a superior cobalt-free perovskite electrocatalyst for solid oxide fuel cells, ACS Appl. Mater. Interfaces 8 (2016) 35308–35314.
[25] R. Raza, Q. Liu, J. Nisar, X. Wang, Y. Ma, B. Zhu, ZnO/NiO nanocomposite electrodes for low-temperature solid oxide fuel cells, Electrochem. commun. 13 (2011) 917–920.
[26] T.H. Shin, J.H. Myung, M. Verbraeken, G. Kim, J.T. Irvine, Oxygen deficient layered double perovskite as an active cathode for CO$_2$ electrolysis using a solid oxide conductor, Faraday Discuss. 182 (2015) 227–239.
[27] B. Savoini, J.M. Santiuste, R. Gonzalez, Optical characterization of Pr^{3+}-doped yttria-stabilized zirconia single crystals, Phys. Rev. B 56 (1997) 5856.
[28] B.L. Treu, W. Fahrenholtz, M. O'Keefe, E. Morris, R. Albers, Effect of phase on the electrochemical and morphological properties of praseodymium-based coatings, ECS Trans. 33 (2011) 53–66.
[29] X. Zhang, Y. Song, F. Guan, Y. Zhou, H. Lv, G. Wang, et al., Enhancing electrocatalytic CO$_2$ reduction in solid oxide electrolysis cell with Ce$_{0.9}$Mn$_{0.1}$O$_{2-\delta}$ nanoparticles-modified LSCM-GDC cathode, J. Catal. 359 (2018) 8–16.
[30] Y.-F. Bu, D. Ding, L. Gan, X.-H. Xiong, W. Cai, W.-Y. Tan, et al., New insights into intermediate-temperature solid oxide fuel cells with oxygen-ion conducting electrolyte act as a catalyst for NO decomposition, Appl. Catal. B 158–159 (2014) 418–425.
[31] M. Zhang, M. Yang, B. Liu, Z. Hou, Y. Dong, M. Cheng, La$_{0.4}$Ce$_{0.6}$O$_{1.8}$–La$_{0.8}$Sr$_{0.2}$MnO$_3$–8mol% yttria-stabilized zirconia composite cathode for anode-supported solid oxide fuel cells, J. Power Sources 175 (2008) 739–748.
[32] N. Hou, P. Li, T. Lv, T. Yao, X. Yao, T. Gan, et al., Sm$_{0.5}$Ba$_{0.5}$MnO$_{3-\delta}$ anode for solid oxide fuel cells with hydrogen and methanol as fuels, Catal. Today 298 (2017) 33–39.
[33] A. Glisenti, M.M. Natile, A. Galenda, PrMnO$_3$ prepared by the citrate gel method, studied by XPS, Surf. Sci. Spectra 16 (2009) 67–74.

[34] M. Guo, J. Lu, Y. Wu, Y. Wang, M. Luo, UV and visible Raman studies of oxygen vacancies in rare-earth-doped ceria, Langmuir. 27 (2011) 3872–3877.

[35] L. Wu, Z. Jiang, S. Wang, C. Xia, $(La,Sr)MnO_3$–$(Y,Bi)_2O_3$ composite cathodes for intermediate-temperature solid oxide fuel cells, Int. J. Hydrogen Energy 38 (2013) 2398–2406.

[36] L. Nie, M. Liu, Y. Zhang, M. Liu, $La_{0.6}Sr_{0.4}Co_{0.2}Fe_{0.8}O_{3-\delta}$ cathodes infiltrated with samarium-doped cerium oxide for solid oxide fuel cells, J. Power Sources 195 (2010) 4704–4708.

[37] Y. Zhang, H. Zhao, Z. Du, K. Świerczek, Y. Li, High-Performance $SmBaMn_2O_{5+\delta}$ Electrode for Symmetrical Solid Oxide Fuel Cell, Chem. Mater. (2019) doi.org/10.1021/acs.chemmater.9b01012.

[38] A.P. Khandale, S.S. Bhoga, An investigation of different $Nd_{1.8}Ce_{0.2}CuO_{4+\delta}$-$Ce_{0.9}Gd_{0.1}O_{2-\delta}$ composite cathodes, Electrochim. Acta 130 (2014) 439–445.

[39] Q. Ni, H. Chen, L. Ge, S. Yu, L. Guo, Investigation of $La_{1-x}Sm_{x-y}Sr_yCoO_{3-\delta}$ cathode for intermediate temperature solid oxide fuel cells, J. Power Sources 349 (2017) 130–137.

[40] Y. Jiao, L. Wang, L. Zhang, W. An, W. Wang, W. Zhou, et al., Direct operation of solid oxide fuel cells on low-concentration oxygen-bearing coal-bed methane with high stability, Energy Fuels 32 (2018) 4547–4558.

[41] B. Shri Prakash, S. Senthil Kumar, S.T. Aruna, Properties and development of Ni/YSZ as an anode material in solid oxide fuel cell: a review, Renewable Sustainable Energy Rev. 36 (2014) 149–179.

[42] I. Tankov, K. Arishtirova, J.M.C. Bueno, S. Damyanova, Surface and structural features of $Pt/PrO_2–Al_2O_3$ catalysts for dry methane reforming, Appl. Catal. A Gen. 474 (2014) 135–148.